

# In-situ study of the impact of temperature and architecture on the interfacial structure of microgels

Steffen Bochenek,<sup>1</sup> Fabrizio Camerin,<sup>2,3</sup> Emanuela Zaccarelli,<sup>2,3</sup> Armando Maestro,<sup>4,5,6</sup> Maximilian M. Schmidt,<sup>1</sup> Walter Richtering,<sup>1</sup> and Andrea Scotti<sup>\*,1</sup>

<sup>1</sup>*Institute of Physical Chemistry, RWTH Aachen University, Landoltweg 2, 52056 Aachen, Germany, European Union*

<sup>2</sup>*CNR-ISC, Sapienza University of Rome, Piazzale Aldo Moro 2, 00185 Roma, Italy, European Union*

<sup>3</sup>*Department of Physics, Sapienza University of Rome, Piazzale Aldo Moro 2, 00185 Roma, Italy, European Union*

<sup>4</sup>*Institut Laue-Langevin ILL DS/LSS, 71 Avenue des Martyrs, 38000 Grenoble, France, European Union*

<sup>5</sup>*Centro de Física de Materiales (CSIC, UPV/EHU) - Materials Physics Center MPC, Paseo Manuel de Lardizabal 5, 20018 San Sebastián, Spain, European Union.*

<sup>6</sup>*IKERBASQUE—Basque Foundation for Science, Plaza Euskadi 5, 48009 Bilbao, Spain, European Union.*

\* E-mail: andrea.scotti@rwth-aachen.de

## Abstract

The structural characterization of microgels at interfaces is fundamental to understand both their 2D phase behavior and their role as stabilizers that enable emulsions to be broken on demand. However, this characterization is usually limited by available experimental techniques, which do not allow a direct investigation at interfaces. To overcome this difficulty, here we employ neutron reflectometry, which allows us to probe the structure and responsiveness of the microgels in-situ at the air-water interface. We investigate two types of microgels with different cross-link density, thus having different softness and deformability, both below and above their volume phase transition temperature, combining experiments with computer simulations of realistic in silico synthesized microgels. We find that temperature only affects the portion of microgels in water, while the strongest effect of the

microgels softness is observed in their ability to protrude into the air. In particular, standard microgels have an apparent contact angle of few degrees, while ultra-low cross-linked microgels form a flat polymeric layer with zero contact angle. Altogether, this study provides an in-depth microscopic description of how different microgel architectures affect their arrangements at interfaces, and will be the foundation for a better understanding of their phase behavior and assembly. **This manuscript has been accepted for publication in Nature Communications (open access). The final version of the manuscript including the Supplementary Information will be available in the future.**

## Introduction

Soft nano- and microgels - cross-linked polymer networks swollen in a good solvent - reveal pe-

cular properties that are different from those of other colloidal systems such as hard nanoparticles, polymers and surfactants.<sup>1-5</sup> The impact of softness, for instance, emerges when micro- and nanogels adsorb at interfaces: they stretch and deform to maximize the coverage of the interface and minimize the interfacial energy.<sup>6-11</sup> At the same time, they do not completely disassemble but remain individual particles, in contrast to other macromolecules such as block copolymer micelles, which irreversibly change their internal conformation upon adsorption at an interface.<sup>12,13</sup>

Nano- and microgels based on poly-*N*-isopropylacrylamide (pNIPAM) have a high interfacial activity<sup>14</sup> and at the same time maintain their thermo-responsiveness once adsorbed to air-,<sup>15-17</sup> liquid-,<sup>18-21</sup> or solid interfaces.<sup>22-25</sup> They can be used to prepare smart emulsions<sup>18,19,26-28</sup> that can be broken on demand as a function of external stimuli such as temperature and pH.<sup>18,19,29-32</sup>

A detailed knowledge of the 3D structure of microgels at an interface is essential to understand fundamental aspects such as their 2D-phase behavior<sup>33-43</sup> or their functionality in emulsion stabilization. While there has been significant progress in studying microgels at solid substrates, in-situ experiments at fluid interfaces are still scarce. A powerful technique to obtain experimental insight into the structure and composition of surfaces and/or thin films with sub-nanometric resolution is specular neutron reflectometry (SNR), which has been employed to study NIPAM-based systems, such as linear polymers and nanogels.<sup>44,45</sup>

Recently, Zielińska et al. probed the structure of pNIPAM nanogels (with diameter smaller than 40 nm) below and at the lower critical solution temperature of pNIPAM of 32 °C.<sup>44,46</sup> They found that nanogels protrude for  $\approx$  2 nanometers in the air phase and form a thick polymeric layer at the interface. After this, two layers of highly solvated pNIPAM were observed. As highlighted in these studies, a key aspect which determines the monolayer structure is represented by the nanogel deformability. More generally, the extent of the microgels' deformation, their final shape, and their phase

behaviour strongly depend on their softness and internal architecture.

It can be expected that size and cross-linker density of the microgels strongly influence the structure of the microgel-covered interface and indeed a transition from particle-to-polymer-like behavior has been observed for ultra-soft microgels adsorbed to solid interfaces.<sup>39</sup> Atomic force microscopy (AFM), cryo-scanning electron (cryoSEM) microscopy, and computer simulations show that adsorbed standard microgels, i.e. microgels with a cross-linker content of few mol %, have a core-corona or fried-egg-like shape when dried, where the fuzzy shell of the microgels forms a thin layer at the interface with the more cross-linked core in the center.<sup>6,8,33,47,48</sup> The core-corona structure gives rise to a rich 2D-phase behavior of the microgel monolayer characterized by a solid-to-solid phase transition.<sup>33</sup> In contrast, AFM measurements demonstrate that ultra-soft microgels have a flat and homogeneous pancake-like structure.<sup>25</sup> Furthermore, depending on the monolayer concentration, they can form both flat films and behave as polymers or as a disordered arrangement of particles.<sup>39</sup>

In this contribution, we address the following questions: Do microgels protrude into the air and if so how far? Is it possible to determine a contact angle for microgels? How are these quantities affected by the cross-linking density and by the collapse of the microgels in the water phase? In particular, we employ SNR to determine in-situ the structure of microgels along the normal to the interface and compare the resulting polymer fraction profiles with those obtained by computer simulations.

We investigate two different types of microgels. The first one is a standard microgel synthesized with a cross-linker content of 5 mol %. This has an architecture characterized by a more cross-linked core and a gradual decrease of the cross-linking density and the polymer segment density towards the periphery. Finally, dangling chains decorate the outer shells.<sup>49</sup> This architecture is a consequence of the fact that the cross-linker agent reacts faster than the monomer during the precipitation polymerization.<sup>50</sup> We prepared two separate batches,

where in one case the isopropyl group of the monomer was deuterated to improve the contrast for neutron reflectivity (NR).

pNIPAM microgels can also be synthesized via precipitation polymerization without addition of a cross-linker agent.<sup>51</sup> The network is formed by self-cross-linking of NIPAM due to transfer reactions.<sup>52</sup> As with the standard microgels, we use a partially deuterated monomer in which the vinyl group is deuterated<sup>52</sup> to increase and vary the contrast in neutron reflectometry. Given the absence of cross-linker agent, these ultra-low cross-linked (ULC) microgels are ultra-soft<sup>53,54</sup> and have an almost uniform, albeit very low, internal density of polymer segments.<sup>39</sup> Nonetheless, such particles remain fundamentally different from linear polymers. For instance, in bulk solution, ULC microgels were found to form colloidal crystals in clear contrast to linear or branched chains.<sup>54,55</sup> Furthermore, their behavior can be tuned between that of polymer and the one of colloidal particle depending on the compression of the monolayer.<sup>39</sup> These microgels also differ from linear polymers once adsorbed at a solid interface where their architecture is the one of ultra-soft disks.<sup>25</sup>

The differences in internal architecture between standard and ULC microgel affect their compressibility and deformability. For instance, the presence of a more cross-linked and denser core inhibits large compression in bulk,<sup>56</sup> whereas the poorly cross-linked network of the ULC microgels is easy to compress in crowded solutions.<sup>53,57</sup> While compressibility is the key aspect for the three-dimensional response of microgels, their deformability is pivotal once they are confined in two dimensions, i.e. onto liquid or solid interfaces.

The analysis of our data shows the effects of the microgel internal architecture on their structure orthogonal to the interface. For both systems, the protrusion in the air and the polymeric layer sitting at the interface are independent of the temperature,  $T$ . Furthermore, simple geometrical considerations on the density profiles combined with the in-plane microgel radius determined by AFM, allow us to determine the apparent contact angle of the adsorbed mi-

crogels. We show that the morphology of ULC microgels is more similar to linear polymers and macromolecules, while standard microgels resemble more closely hard colloids.

## Results

### Microgel structure in bulk solution

The ratio between the hydrodynamic radius in the swollen and collapsed state - swelling ratio - is a good measurement of the softness of the microgel network: The larger this ratio, the softer the microgel.<sup>58-60</sup> All microgels studied here have a comparable hydrodynamic radius at 20 °C, see Table 1 and Supplementary Fig. 1a. They do however exhibit different swelling ratios, see Supplementary Fig. 1b.

Table 1: Characteristic lengths of the individual pNIPAM based microgels below and above their VPTT.

Name	T	$R_h$	$R_{\text{SANS}}$	$R_{\text{SANS,c}}$	$2\sigma_{\text{SANS}}$	$2R_{2\text{D}}$	$2R_{2\text{D,c}}$	$h_{2\text{D}}$
	(°C)	(nm)	(nm)	(nm)	(nm)	(nm)	(nm)	(nm)
5 mol% D0	20	150	151	32	119	688	360	21
5 mol% D0	40	85	72	59	13	651	289	26
5 mol% D7	20	153	120	33	87	-	-	-
5 mol% D7	40	72	62	57	5	-	-	-
ULC D3	20	138	134	53	81	733	-	3
ULC D3	40	54	56	41	15	689	-	4

Hydrodynamic radius in water,  $R_h$ , radius from SANS in  $\text{D}_2\text{O}$ ,  $R_{\text{SANS}} = R_{\text{SANS,c}} + 2\sigma_{\text{SANS}}$  where  $R_{\text{SANS,c}}$  is the core radius in bulk and  $2\sigma_{\text{SANS}}$  is the fuzziness of the shell in bulk determined by SANS.  $2R_{2\text{D}}$  is the interfacial (dry) diameter and  $2R_{2\text{D,c}}$  is the interfacial (dry) diameter of the core.  $h_{2\text{D}}$  is the maximum height once adsorbed (dry). The last three quantities are determined by AFM, see Supplementary Figs. 3 and 4. The values including the errors are given in Supplementary Table 1.

For the hydrogenated 5 mol% cross-linked standard pNIPAM microgels, 5 mol% D0, the swelling ratio is  $1.76 \pm 0.03$ . For the deuterated pNIPAM microgels synthesized with the same amount of cross-linker - 5 mol% D7 - the swelling ratio is  $2.12 \pm 0.04$ . Finally, the swelling ratio of the deuterated pNIPAM ULC microgels, ULC D3, is  $2.56 \pm 0.05$ . This confirms that

the ULC microgels are the softest, according to this parameter.

Small-angle neutron scattering (SANS) is used to determine the characteristic lengths of the microgels, such as total radius,  $R_{\text{SANS}}$ , radius of the more cross-linked core,  $R_{\text{SANS,c}}$ , and extension of the fuzzy shell,  $2\sigma_{\text{SANS}}$ . The values of these quantities are determined fitting the form factors with the fuzzy-sphere model<sup>49</sup> and are reported in Table. 1. The data and the fits in Supplementary Figs. 2a-d confirm the different internal architecture between standard and ULC microgels.

We note that the main effects of selective deuteration and of using deuterated solvents is to shift the VPTT of pNIPAM to a higher temperature.<sup>61-64</sup> However, at the lowest and highest temperatures measured, the microgels are in the fully swollen and collapsed state (see Supplementary Figs. 1c and 2a-d), respectively, allowing for an appropriate comparison of the different architectures.

## Standard Microgels at the interface

For each monolayer of hydrogenated and deuterated microgels studied here, the intensities of the reflected neutrons,  $R(Q)$ , were recorded as a function of momentum transfer normal to the interface,  $Q$ , in two isotopic contrasts:  $\text{D}_2\text{O}$  and air contrast matched water (ACMW). The latter consists in a mixture of  $\text{D}_2\text{O}$  and  $\text{H}_2\text{O}$  (8.92% v/v), which matches the scattering length density (SLD) of air ( $b_{\text{air}} = 0 \cdot 10^{-4} \text{ nm}^{-2}$ ), and therefore only the polymer contributes to the reflected signal of the curves in Figures 1a and b.  $R(Q)$  for the same microgels, measured in  $\text{D}_2\text{O}$  as sub-phase, is plotted in the insets of the Figures 1a and b. In this case, when a neutron beam is reflected from air at  $\text{D}_2\text{O}$ , which has a higher SLD ( $b_{\text{D}_2\text{O}} = 6.36 \cdot 10^{-4} \text{ nm}^{-2}$ ) or a lower refractive index  $n = 1 - \lambda^2/2\pi b$  (with  $\lambda$  the neutron wavelength), respectively, total reflection occurs below a critical value of the momentum transfer  $Q_c = 0.16 \text{ nm}^{-1}$ . Above this value the reflectivity decays as a function of  $Q^4$ .

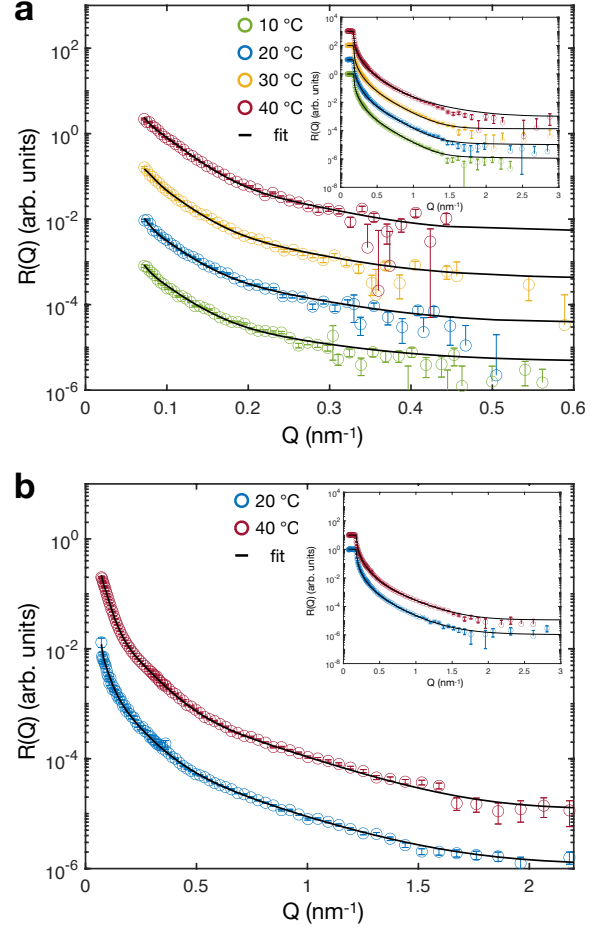


Figure 1: Reflectivity curves of 5 mol% cross-linked microgels at different temperatures. **a** Reflectivity curves, reflectivity,  $R(Q)$ , versus momentum transfer,  $Q$ , of pNIPAM microgels at the air-ACMW interface and corresponding fits. **b** Reflectivity curves of D7-NIPAM microgels at the air-ACMW interface with fits. Insets: Reflectivity curves at air- $\text{D}_2\text{O}$  interfaces. The curves are shifted in y-direction for clarity. The unshifted curves are shown in Supplementary Figs. 6a and b. The error bars represent the statistical errors on  $R(Q)$ .

The samples studied here yielded laterally homogeneous interfaces on the length scale of the in-plane neutron coherence length, on the order of several microns.<sup>65</sup> This implies that the measured SNR can be correlated with the averaged SLD depth profile across the interface delimited by this coherence length and, therefore, the in-situ structure of the microgels as a function of the distance from the interface  $z$  can be determined. This is done by fitting the reflectivity

curves with a model consisting in different layers characterized by a thickness,  $d$ , a roughness,  $\sigma$ , and a SLD,  $b$ . The latter contains information on the atomic density of the NIPAM molecules and, therefore, is linked to the polymer concentration and solvation of the different layers (see Methods section for further details). Here, we find that a model composed by 4 layers is the most suitable to describe the density profile of the standard pNIPAM microgels perpendicular to the plane of the interface where the layers 1-to-4 are sandwiched between the bulk air (layer 0) and the bulk solvent (background layer).

The length and width of the slab are delimited by the illuminated area that is roughly  $10^9$  times the interfacial diameter of the measured microgel. Therefore, in contrast to microscopy-based techniques, our measurements probe a statistically significant ensemble of microgels. We fit the  $R(Q)$ -curves of the same sample at the same temperature for both contrasts simultaneously to reduce the number of free parameter. The best fits are shown by the black full lines in Figures 1a and 1b. The parameters of the fits are reported in Table 2. The use of models with a smaller number of layers cannot reproduce the experimental data or it leads to density profile inconsistent with previous studies,<sup>6,10,35,66–69</sup> see Supplementary Figs. 7a-c.

Additionally, to verify the validity of the four slab-models, the data for the deuterated microgels at 20 °C have been fitted using a continuous variation of the SLD profile sliced into many ( $> 1000$ ) thin layers of 1.5 Å thickness. As shown in the Supporting Information (Supplementary Fig. 10a and b), the fit leads to identical results and, therefore, validates the findings from the four slab-models used. From this discussion, it is clear that the model employed here can reproduce the data with the due accuracy and the lowest number of free fitting parameters.

Figures 2a and b show the polymer fraction normal to the interface ( $z$ -distance) of the hydrogenated (5 mol% D0) and deuterated (5 mol% D7) microgels, respectively. These curves are calculated from the SLD profiles obtained from the fits and shown in Supplementary Figs. 8a and b.

We note that the extension of the dangling, highly hydrated polymeric chains at the end of the swollen microgels is accounted considering the roughness between the last layer and the background, i.e. equals  $2\sigma_{\text{bkg}}$ . The profiles of the polymer fraction normal to the interface show that the microgels deswell in the vertical direction with increasing temperature. The total film thickness  $d_{\text{total}} = d_1 + \dots + d_N + 2\sigma_1 + 2\sigma_{\text{bkg}}$  is reported in the last column of Table 2.

Below the VPTT, the 5 mol% D0 microgels are fully swollen and have a  $d_{\text{total}}$  in between  $210 \pm 6$  and  $220 \pm 5$  nm. Once the microgels are collapsed at 40 °C, they are deswollen and have a thickness of  $d_{\text{total}} = (140 \pm 5)$  nm. In the literature, a very similar value of the thickness was measured for the same microgels in the swollen and collapsed state with ellipsometry.<sup>34</sup> Also the deuterated microgels show the deswelling with temperature. The thickness of the monolayer in the swollen and the deswollen state is  $d_{\text{total}} = 245 \pm 14$  nm and  $d_{\text{total}} = 160 \pm 2$  nm, respectively; see Table 2.

In our model, the protrusion of the microgel into the air is  $d_p = d_1 + 2\sigma_1$  and is calculated using the values given in Table 2. For clarity, we have shifted the position of the polymer profiles along the  $z$ -distance to have this protrusion layer at negative distances from the interface, Figures 2a and b. The unshifted polymer fraction profiles are shown in the Supporting Information, Supplementary Fig. 9a and b.

At 20 °C, the 5 mol% D0 and 5 mol% D7 microgels protrude approximately  $30 \pm 2$  and  $37 \pm 2$  nm into the air, respectively. This corresponds to about 10% of the diameter of the swollen microgels in solution or 15% of their  $d_{\text{total}}$ . The protrusion into the air phase does not change significantly with increasing temperature. Geisel et al. determined a protrusion height below 70 nm for microgels of similar size. They noted that this value is the maximum protrusion height according to geometrical calculations from the cryoSEM images and has to be interpreted as an upper limit.<sup>6</sup>

The estimated values of  $d_p$  allow us to calculate the apparent contact angles of the microgels assuming a simple orthogonal triangle. To this aim, we make use of the total inter-

Table 2: Parameters of the 4-layers fit for the 5% cross-linked microgels in Figure 1.

T	Layer 1			Layer 2			Layer 3			Layer 4			Background	
(°C)	$d_1$ (nm)	$\sigma_1$ (nm)	$b_1$ ( $10^{-6} \text{ \AA}^{-2}$ )	$d_2$ (nm)	$\sigma_2$ (nm)	$b_2$ ( $10^{-6} \text{ \AA}^{-2}$ )	$d_3$ (nm)	$\sigma_3$ (nm)	$b_3$ ( $10^{-6} \text{ \AA}^{-2}$ )	$d_4$ (nm)	$\sigma_4$ (nm)	$b_4$ ( $10^{-6} \text{ \AA}^{-2}$ )	$\sigma_{\text{bkg}}$ (nm)	$d_{\text{total}}$ (nm)
5 mol% D0 Microgels, $b_{\text{theo}} = 0.93 \cdot 10^{-6} \text{ \AA}^{-2}$														
10	14	8	0.06	2.1	0.7	0.32	4.4	0.4	0.14	122	3.5	0.06	31	220
20	14	8	0.06	2.1	0.7	0.31	4.3	0.8	0.19	117	3.5	0.07	28	210
30	14	8	0.08	2.2	1.0	0.35	4.7	0.6	0.20	99	4.0	0.08	29	194
40	14	7	0.10	2.7	0.5	0.35	6.8	1.0	0.23	48	3.2	0.10	26	140
5 mol% D7 Microgels, $b_{\text{theo}} = 4.78 \cdot 10^{-6} \text{ \AA}^{-2}$														
20	16	11	0.1	2.3	0.5	1.58	3.0	0.2	0.49	136	3.4	0.21	33	245
40	16	8	0.2	2.6	0.2	1.73	4.7	0.3	0.62	66	2.6	0.26	27	160

$d_i$  is the thickness of a layer with the scattering length density  $b_i$ .  $\sigma_i$  is the roughness between a layer and the layer above it.  $d_{\text{total}}$  is the total film thickness and  $\sigma_{\text{bkg}}$  is the roughness between the last layer and the background. The Uncertainties from the fits are given as errors in Supplementary Table 2.

facial diameter  $2R_{2D}$  of the individual microgels determined by AFM measurements, see Table 1. The apparent contact angle,  $\theta_{C,\text{app}} = \arctan(d_p/R_{2D})$  is found to be approximately  $5^\circ$  at 20 and  $40^\circ\text{C}$ . Since the corona of the microgels is expected to form a flat layer within the interfacial plane, the interfacial diameter of the core,  $2R_{2D,c}$ , can be used instead. This results in  $\theta_{C,\text{app}}$  of  $9^\circ$  and  $11^\circ$  at 20 and  $40^\circ\text{C}$ , respectively.

The second region is a thin, polymer-rich layer lying at  $z = 0$  ( Figures 2a and b). In our model, this region is described by layer 2 in Table 2. We assume slabs parallel to the interface and, therefore, we only determine an average SLD which is proportional to the average polymer fraction at the interface. Similarly to the protrusion of the microgels in air, also this polymer-rich layer is temperature independent and has a constant volume fraction of  $\approx 0.33$ , as indicated by the constant values of SLD reported in Table 2. The high polymer content in these regions implies that the network expelled a significant amount of solvent compared to the solvated part in water. Therefore, we can compare the thickness of these two layers ( $\approx 40 \text{ nm}$ ) to the length of the collapsed shell at high temperatures in bulk, see Table 1, which is found to be much smaller than the layers thickness. From this, we can infer that also a part of the more cross-linked core protrudes into the air, as shown in Figure 2 and in the sketch in Figure 3a-c.

Our model also reproduces the portion of a microgel in the aqueous phase, i.e. the third region, as shown by the polymer fractions at  $z > 0$  in Figures 2a and b. This portion of the microgel is described by the third and fourth layers, and the corresponding parameters are reported in Table 2. Its extension is calculated as  $d_{\text{water}} = d_3 + d_4 + 2\sigma_{\text{bkg}}$  and shows the strongest reaction to a change of temperature. For the hydrogenated microgels,  $d_{\text{water}}$  goes from  $178 \pm 5$  to  $106 \pm 5 \text{ nm}$  when temperature increases from 20 to  $40^\circ\text{C}$ . A change in  $d_{\text{water}}$  from  $205 \pm 6$  to  $125 \pm 2 \text{ nm}$  for the same temperature increase is determined for the 5 mol% D7 microgels. This collapse is accompanied by an increase of the polymer fraction in the layers 3 and 4 for both microgels as indicated by the increases in the values of  $b_i$ . We note that both below and above the VPTT, the values of  $d_{\text{water}}$  are smaller than the hydrodynamic diameters of the swollen and collapsed microgels in bulk,  $2R_h$  in Table 1. This observation, combined with the large values of the interfacial diameters, indicates a strong deformation of the adsorbed microgels, see Figure 3a-c. On the other hand, the swelling ratio in 2D, defined as the ratio between  $d_{\text{water}}$  at 20 and  $40^\circ\text{C}$ , is found to be  $1.68 \pm 0.09$  and  $1.65 \pm 0.05$  for the hydrogenated and deuterated 5 mol% cross-linked microgels, respectively. These values are smaller than the corresponding ratios in 3D, implying that the adsorption leads to a stiffening of the polymeric networks swollen in

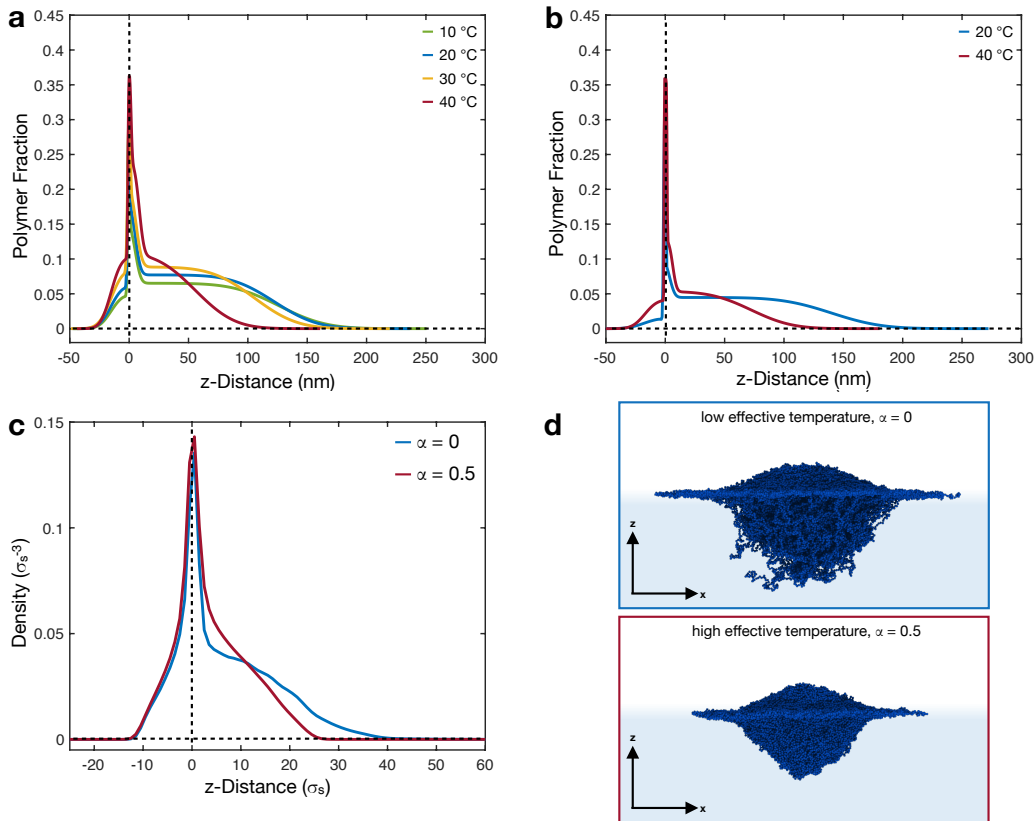


Figure 2: Structure of 5 mol% cross-linked microgels at liquid interfaces. Polymer fractions of the adsorbed 5 mol% D0 **a** and 5 mol% D7 **b** microgels at different temperatures. **c** Density profiles of simulated microgels at different effective temperatures, corresponding to  $\alpha = 0, 0.5$ . Horizontal and vertical dashed lines are guidelines for the eyes and represent zero polymer fraction/density and zero  $z$ -distance from the interface, respectively. Negative values of  $z$  represent the air phase and positive values represent the water phase. **d** Simulation snapshots showing the side perspective of an adsorbed standard microgel for  $\alpha = 0, 0.5$ . Solvent particles are not shown for visual clarity.

water, as also found in computer simulations.<sup>37</sup> Furthermore, provided both microgels have the same 2D swelling ratio, the 5 mol% cross-linked standard microgels have similar softness at the interface, whereas in bulk the deuterated ones appear to be slightly softer.

We also note that the slight difference in polymer fraction in the water phase between deuterated and hydrogenated nanogels depends on the fact that they have slightly different masses and molecular weights  $M_w$ . Combining viscosimetry measurements and dynamic light scattering measurements,<sup>70</sup> we found that the 5 mol% D7 microgels have a mass of  $6.3 \pm 0.6 \cdot 10^{-19}$  kg ( $M_w = 3.8 \pm 0.4 \cdot 10^8$  gmol<sup>-1</sup>), while the 5 mol% D0 microgels have a mass of  $7.7 \pm 0.7 \cdot 10^{-19}$  kg ( $M_w = 4.6 \pm 0.4 \cdot 10^8$  gmol<sup>-1</sup>).

The conformation of the regular microgel at the interface is in excellent agreement with numerical simulations. In this case, microgels are synthesized in silico through the self-assembly of patchy particles.<sup>37,71</sup> The resulting polymer network is disordered and accounts for a higher concentration of cross-linkers in the core of the particle, with a bulk density profile that progressively rarefies in the outer corona. The microgel is embedded within two different types of immiscible solvents, mimicking air and water, which gives rise to a surface tension similar to experiments. In this way, the simulated microgel spontaneously acquires the typical fried-egg-like shape. More details on the assembly process and on the simulations at the interface can be found in the Methods section.

In order to compare with the experimental profiles of the microgel parallel to the plane of the interface, we calculate the numerical number density profiles by dividing the simulation box into three-dimensional slabs along the  $z$ -direction, i.e. orthogonally to the interfacial plane. In this way, we have direct access to the polymer network, without any interference given by the presence of the solvent. The resulting profiles are reported in Fig. 2c for two different effective temperatures.

The three regions described experimentally are also present in the numerical profiles. At all temperatures, we detect the presence of a protrusion into the air phase and a polymer layer lying on the interface. As shown by the snapshots reported in Fig. 2d, the protrusion is given by the fact that the more cross-linked core cannot fully expand, as it happens for the corona, on the interfacial plane. In fact, the corona creates the second part of the density profile that is characterized by a pronounced peak at the interface. The polymer network accumulates onto the interface to reduce the surface tension between the two fluids as much as possible. The third region of the profile is inside the aqueous phase. As in the experiments, this region is most affected by temperature. While at low temperatures a large portion of the microgel protrudes significantly into the aqueous phase, at high temperatures the microgel tends to assume a more spherical and compact shape, contracting the polymer chains toward the interfacial plane. The consistency between simulations and experiments also allows us to confirm the robustness of the four layers fitting model used in experiments.

## ULC microgels at the interface

The reflectivity curves of deuterated ULC microgels at the air-ACMW interface are shown in Figure 4. In the inset, the measurements with pure  $D_2O$  as sub-phase are shown. In contrast to standard microgels, a three-layer model can successfully fit the data (solid lines in Figure 4). The fit parameters are obtained by fitting neutron reflectivity (NR) curves of the same sample at the same temperature simultaneously for

both contrasts. Their values are reported in Table 3.

Once more, we checked the validity of the three-layer model by comparing the results from a fit with a model consisting of a continuous variation of the SLD with many thin layers. In the Supplementary Information, it is shown that the results from the two models are identical (Supplementary Figs. 10c and d). This further demonstrates that a slab model including a Gaussian error function can successfully reproduce the experimental NR data of ULC microgels with the smallest number of free parameters.

The structure of the deuterated ULC microgels as a function of the distance to the interface is described by the shifted and unshifted polymer fraction profiles in Figure 5a and Supplementary Fig. 9c, respectively. At 20 °C, the length of the protrusion of ULC microgels into air is  $d_p = 8 \pm 3$  nm. This is less than 3% of the ULC swollen diameter in solution and approximately 5% of the total thickness of the ULC,  $d_{\text{total}} = 157 \pm 7$  nm, see Table 3. Similarly to standard microgels, the ULC protrusion into air does not change once temperature rises above the VPTT. Another similarity with the standard microgels is the presence of a dense layer of polymer sitting on the interface of  $\approx 3$  nm. Adding the length of the protrusion in air,  $d_p$ , to this extension, we obtain  $\approx 11 - 15$  nm which is consistent with the extension of the collapsed fuzzy shell measured by SANS for the D3-ULC microgels, see Table 1. This indicates that, in contrast to standard microgels, only the collapsed external shell protrudes into air and lies on the interface, as shown in Figure 5 and sketched in Figure 3d-f.

The third region of the ULC microgels has a lower polymer fraction (below 0.04, Fig. 5a) compared to the standard microgels (above 0.05 Figs. 2a and b) below the VPTT. Unfortunately, due to the resolution of NR and the fact that we average the SLD over the entire monolayer, it is not possible to finely resolve the structure of the collapsed ULC. Above the VPTT, the polymer fraction in the third region of the collapsed ULC is estimated from the value of  $b_3$  to be  $\approx 0.003$ . This small value



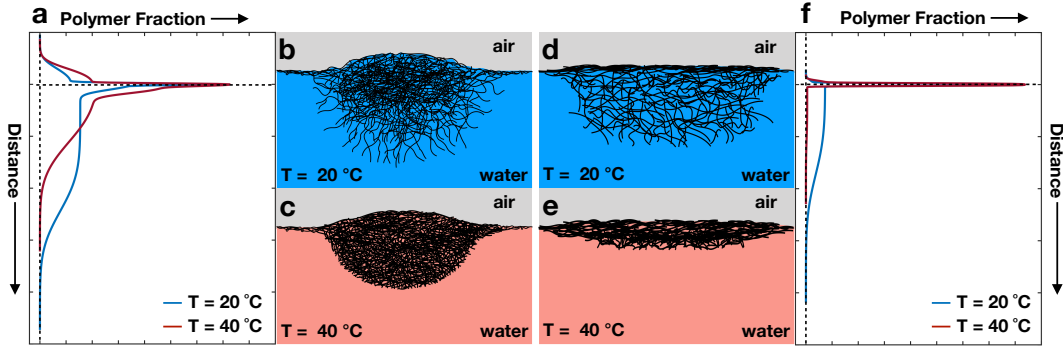


Figure 3: Sketch of the adsorbed microgels. Panel **a** shows the vertical profiles of standard microgels and **f** the vertical profiles of ULC microgels below and above the VPTT. Their corresponding shapes are outlined in **b-e**. The shapes are based on the combination of our polymer fraction profiles, simulations and AFM measurements at the liquid-solid interface from the literature.<sup>25</sup>

Table 3: Summary of the model fits of the reflectivity curves of the ULC D3 microgels in Figure 4.

T	Layer 1			Layer 2			Layer 3			Background	
(°C)	$d_1$ (nm)	$\sigma_1$ (nm)	$b_1$ ( $10^{-6} \text{ \AA}^{-2}$ )	$d_2$ (nm)	$\sigma_2$ (nm)	$b_2$ ( $10^{-6} \text{ \AA}^{-2}$ )	$d_3$ (nm)	$\sigma_3$ (nm)	$b_3$ ( $10^{-6} \text{ \AA}^{-2}$ )	$\sigma_{\text{bkg}}$ (nm)	$d_{\text{total}}$ (nm)
ULC D3 Microgels, $b_{\text{theo}} = 2.57 \cdot 10^{-6} \text{ \AA}^{-2}$											
20	3	2	0.04	2.2	0.4	1.01	86	0.4	0.09	30	157
30	3	2	0.070	2.4	0.4	1.08	64	0.2	0.09	26	125
36	3	2	0.110	2.6	0.2	1.08	61	0.2	0.05	25	120
40	3	1	0.120	2.7	0.4	1.08	52	0.4	0.008	15	89

$d_i$  is the thickness of a layer with the scattering length density  $b_i$ .  $\sigma_i$  denotes the roughness between a layer and the layer above it.  $d_{\text{total}}$  the approximated total film thickness and  $\sigma_{\text{bkg}}$  the roughness between the last layer and the background. The uncertainties from the fits are given as errors in Supplementary Table 3.

might result from the average between regions with no polymer and denser globules of collapsed microgels around the few cross-linking points. Such globules have been observed by AFM on re-hydrated ULC microgels adsorbed onto solid interfaces after transferring from a Langmuir-Blodgett trough.<sup>38</sup>

As for the regular microgels, we can use the estimated  $d_p$  and the 2D radius of the ULC microgels to compute their apparent contact angles. The resulting angles are negligible,  $\approx 1^\circ$ , at both temperatures. This behavior is close to what one can expect for macromolecules adsorbed at interfaces in contrast to colloidal particles. This is consistent with recent literature on these ultra-soft microgels. Indeed, it has been shown that, due to their high compressibility and deformability,<sup>25,54</sup> these microgels show

the typical behavior of polymers. For instance, their bulk viscosity does not diverge in proximity of the glass transition but at much higher concentrations, indicating a high degree of deformability.<sup>72</sup> Also at the interface it has been shown that, depending on their concentration, they can cover the interface uniformly as a linear polymer or create a disordered array of individual particles as hard colloids.<sup>39</sup>

To gain more information on the adsorbed ULC microgels, we also performed computer simulations of such system. The corresponding density profiles and simulation snapshots are reported in Figure 5b and 5c, respectively. At both effective temperatures, the ULC microgels show a flat profile. The polymer network appears to be equally distributed across the interface, with only a slight preference for the wa-

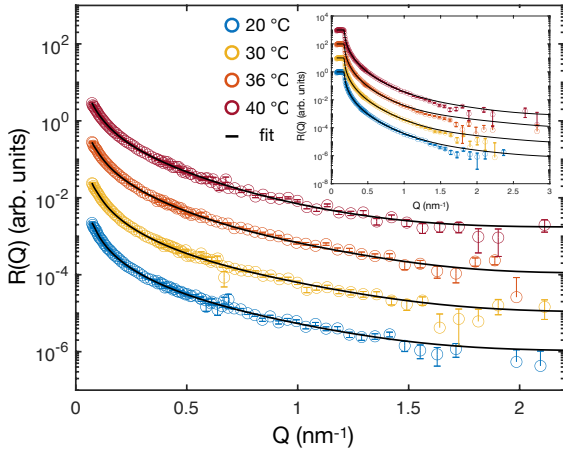


Figure 4: Reflectivity curves of ULC D3 microgels at different temperatures. Reflectivity,  $R(Q)$ , versus momentum transfer,  $Q$ , at the air-ACMW interface. The fits are shown by continuous lines. Inset: Reflectivity curves at air-D<sub>2</sub>O interfaces. The curves are shifted in y-direction for clarity. The unshifted curves are shown in Supplementary Figs. 6c. The error bars represent the statistical errors on  $R(Q)$ .

ter phase. Consistently with experiments, no effect of temperature change is observed for the fraction of polymer in the air side and on the plane of the interface. Furthermore, as in the experiment, the contact angle for the ULC microgels is virtually zero.

For standard microgels, the presence of the well-defined core generates a noticeable dense protrusion into the aqueous phase (Fig. 2a); for the ULC microgels, the amount of polymer in water is considerably lower (Fig. 5a). The ULC microgels extend into the aqueous phase for  $d_{\text{water}} = d_4 + 2\sigma_{\text{bkg}} = 144 \pm 8$  nm at  $T = 20^\circ\text{C}$ . Furthermore, they remain thermo-responsive and their extension in water decreases to  $d_{\text{water}} = 83 \pm 3$  nm when temperature changes from 20 to  $40^\circ\text{C}$ . The 2D swelling ratio equals  $1.7 \pm 0.1$ , a value much smaller than the corresponding 3D ratio and comparable to the swelling ratio of the standard microgels in 2D. This implies that also ULC microgels experience a significant stiffening of the polymeric network in water due their the large deformation. This takes place both in the lateral and in the vertical directions, as indicated by their

large in-plane diameter and by the fact that  $d_{\text{water}} \ll 2R_h$ , see Table 1. Furthermore,  $d_{\text{water}}$  at  $40^\circ\text{C}$  is slightly larger than the region with more homogeneous polymer distribution of the collapsed ULC as measured by SANS, see Table 1. Therefore, we can assume that this region does not protrude into the air as shown in the sketch in Figure 3d-e.

While the experimental and numerical descriptions of ULC microgels agree regarding the microgel portion which protrudes in air and sits onto the interface, there is a difference in what we observe in the water phase. This is most likely generated by the presence of few dangling chains that do not absorb on the plane of the interface and, therefore, protrude into the aqueous phase. The reason why this protrusion is not observed in the numerical profiles is most likely due to the small size of the simulated microgel. In fact, the number of monomers and the minimal percentage of cross-linkers employed for the *in silico* synthesis cause the microgel to be highly extended allowing for all simulated monomers to absorb at the interface. On the contrary, we expect that a significantly larger microgel would have enough monomers to form a plain layer at the interface so that some chains would be desorbed into the aqueous phase, as is the case in experiments. Nevertheless, at present, this is computationally unfeasible due to the huge number of particles that would be involved in an explicit solvent simulation with such a large-sized microgel. For the same reason, an accurate quantitative comparison between numerical and experimental density profiles is, at the moment, out of reach.

## Discussion

In this article, we used neutron reflectometry and computer simulations to probe the structure of microgels orthogonal to the air-water interface, below and above the VPTT. The advantage of neutron reflectometry is that it allows to probe the structure of a statistically significant ensemble of microgels *in-situ* at the interface. Using NR, we can directly measure the protrusion of the microgels in the

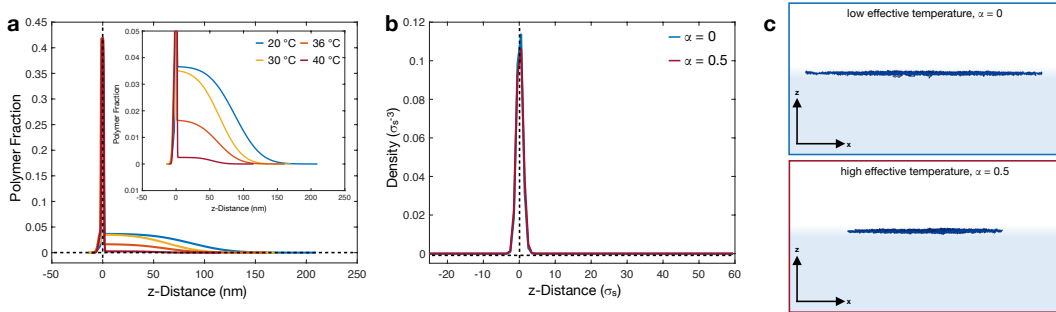


Figure 5: Structure of ULC microgels at liquid interfaces. **a** Results of the fits of the experimental data for the ULC D3 microgels. Inset: Zoom of polymer fraction profiles. **b** Density profiles of simulated ultra-low cross-linked microgels at different effective temperatures, corresponding to  $\alpha = 0, 0.5$ . Horizontal and vertical dashed lines are guidelines for the eyes and represent zero polymer fraction and zero z-distance from the interface, respectively. Negative values of z represent the air phase and positive values represent the water phase. **c** Simulation snapshots showing the side perspective of an adsorbed ULC microgel for  $\alpha = 0, 0.5$ . Solvent particles are not shown for visual clarity.

air and estimate how it changes with temperature. Microscopy-based techniques such as transmission X-ray microscopy (TXM) or cryoSEM are usually limited by the small number of observed particles, the size of the particles, an observation direction perpendicular to the interface, and complicated sample preparation.<sup>6,8,10,66</sup> The latter makes it particularly difficult, for example, to observe the effect of temperature on the swelling of microgels.

In the future, super-resolved fluorescence microscopy techniques, which in principle can resolve sizes below 30 nm,<sup>5</sup> could also be used at the air-water interface to obtain complementary data. To date, however, even these techniques are limited by the spatial resolution in the z-direction that is  $\approx 60$  nm<sup>73</sup> and by the difficulties in the analysis of the point clouds generated by the blinking of the dyes.<sup>74,75</sup>

For both 5 mol% cross-linked and ultra-low cross-linked microgels, we find that the portion of microgels protruding in air is insensitive to changes in temperature (Figs. 3a and f). Concerning standard microgels, the more cross-linked core is found to partially protrude in the air, leading to an estimate of the apparent contact angle of a few degrees (Figs. 3b and c). This value is significantly smaller than the angle estimated using cryoSEM and TXM of microgels protruding into different n-alkanes.<sup>6,66</sup>

The reason for this discrepancy is probably that the cryoSEM estimates were limited either by the smallest angle employed, which was about 30 °,<sup>6</sup> or by the size of the employed microgels.<sup>66</sup>

In contrast, ULC microgels form a flat polymer layer that protrudes only a few nanometers into the air, resulting in a nearly null apparent contact angle (Figs. 3d and e). We also note that the length of such a layer is approximately equal to the extent of its collapsed fuzzy shell (Table 1), supporting the idea that only this part protrudes into the air. Again, since these microgels are ultra-soft and extremely deformable, they stretch as much as possible after adsorption at the interface to minimize the interfacial energy. This behavior is consistent with the experiments of Richardson and co-workers that used neutron reflectivity to probe linear pNIPAM solutions and nanogels with a mesh-size comparable to their dimensions and, therefore, highly stretchable at the interfaces.<sup>44,45</sup> Above the pNIPAM LCST, the collapsed film protrudes about 4 nm into air,<sup>45</sup> which is practically the same as the protrusion height estimated here for the ULC microgels. These observations are consistent with the fact that the adsorbed ULC microgels behave more like linear polymers rather than rigid particles.<sup>39</sup>

The present study can also contribute to the

current debate on the role and importance of capillary interactions for microgels adsorbed at the interface, which seem to be significant only for large particles.<sup>76,77</sup> Indeed, the strength of capillary interactions depends on the size of the particles, the density difference between the particles and the liquid, and the contact angle.<sup>78</sup> Therefore, our measurements reinforce the idea that for small microgels with low contact angle, such as the one investigated here, capillary forces are negligible.

Finally, our work is important to shed light on the collective behavior of microgels at interfaces. The differences we highlighted in the structure may be relevant for a more comprehensive understanding of microgels' effective interactions, paving the way for a better description of their 2D assembly and for a clever design of their applications such as emulsion stabilizers.

Recent literature has also shown that the substitution between air and alkanes, such as decane, only slightly changes the stretching of the microgels at the interface.<sup>36</sup> This is due to high interfacial tension of the two systems and the insolubility of the microgels in the alkane/oil. However, at lower interfacial tensions, a greater reduction in the spreading of the microgels is observed.<sup>79</sup> Therefore, we expect that our results on the protrusion of the microgels into the hydrophobic phase and the observed difference between ULC and standard microgels at an alkane/(oil)-water interface will not change qualitatively.

## Methods

### Synthesis

Standard 5 mol% D0 (SFB985\_B8\_SB\_M000325), 5 mol% D7 (SFB985\_A3\_MB\_M000238), and ULC D3 (SFB985\_A3\_MB\_M000301) Microgels were synthesized by precipitation polymerization.<sup>34,52,56,57</sup> The main monomers for all microgels were NIPAM (D0) or deuterated NIPAM, in which three (D3) or seven (D7) hydrogen atoms have been exchanged by deuterium. The deuterated monomers were

obtained from Polymer Source, Canada, hydrogenated monomers were obtained from Acros Organics, Belgium. Surfactants, sodium dodecyl sulfate (SDS) or cetyltrimethylammonium bromide (CTAB), were added during the synthesis to control the size polydispersity and final microgel size. Briefly, for the three different synthesis, 5.4546 g of D0-NIPAM (5 mol% D0 microgels), or 1.5072 g of D7-NIPAM (5 mol% D7 microgels), or 1.0093 g of D3-NIPAM (ULC D3 microgels) were dissolved in 330 mL, 83 mL, and 70 mL double-distilled water, respectively. For the 5 mol% microgels 0.3398 g (5 mol% D0) or 0.1021 g (5 mol% D7) of the cross-linker *N,N'*-methylenebisacrylamide (BIS) were added. No additional cross-linker was included during the synthesis of the ULC D3 microgels. The reaction flask of the 5 mol% D0 microgels contained additionally 0.1474 g of *N*-(3-aminopropyl) methacrylamide hydrochloride (APMH) as co-monomer. The monomer solutions were purged with nitrogen under stirring and heated to 65 °C (5 mol% D0), 70 °C (5 mol% D7) and 70 °C (ULC D3). The initiators and the surfactants were dissolved in a few milliliters of double-distilled water in separated vessels and degassed for at least one hour. For the deuterated 5 mol% D7 and ULC D3 microgels 0.372 g and 0.0506 mg of potassium peroxydisulfate (KPS) and 0.202 g and 0.0277 g of SDS were used, respectively. For the 5 mol% D0 microgels, 0.2253 g 2,2'-Azobis-(2-methyl-propionamidin) dihydrochlorid (V50) and 0.0334 g of CTAB were used. After adding the surfactant to the reaction flask, the polymerization was initiated by injecting the dissolved initiators. The reactions were carried out for 4 h at the given temperatures and under constant nitrogen flow and stirring. The obtained microgels were purified by threefold ultra-centrifugation and re-dispersion in fresh double-distilled water. Lyophilization was applied for storage for all microgels.

### Dynamic light scattering

A laser with vacuum wavelength  $\lambda_0 = 633$  nm was used to probe diluted suspensions of the different microgels in water and heavy water. The

temperature was change from 20 °C to 50 °C in steps of 2 °C using a thermal bath filled with toluene to match the refractive index of the glass. The momentum transfer  $Q = 4\pi/\lambda \sin \theta$ , was changed by varying the scattering angle,  $\theta$ , between 30 and 130 degrees, in steps of 5 degrees.

## Small-angle neutron scattering

SANS experiments were performed at the KWS-2 instrument operated by the JCNS at the MLZ, Garching, Germany, and at the D11 instrument at the Institut Laue-Langevin (ILL, Grenoble, France). For the KWS-2 the  $q$ -range of interest was covered by using a wavelength for the neutron beam of  $\lambda = 0.5$  and 1 nm and three sample-detector distances: 20, 8 and 2 m. The detector is a 2D- $^3\text{He}$  tubes array with a pixel-size of 0.75 cm and a  $\Delta\lambda/\lambda = 10\%$ . For the D11 three configurations were used: sample detector distance,  $d_{\text{SD}} = 34$  m with  $\lambda = 0.6$  nm;  $d_{\text{SD}} = 8$  m with  $\lambda = 0.6$  nm; and  $d_{\text{SD}} = 2$  m with  $\lambda = 0.6$  nm. Due to the velocity selector, the resolution in  $\lambda$  was 9%. The D11 is equipped with a  $^3\text{He}$  detector with a pixel size of 7.5 mm.

## Compression isotherms and depositions

Gradient Langmuir-Blodgett type deposition<sup>33,34,36</sup> from air-water interfaces were performed to study the mechanical properties of the microgels and microgel monolayers and visualize them ex-situ. The Langmuir-Blodgett trough was made from polyoxymethylene (POM) and was equipped with two movable POM barriers. For each deposition, the trough was carefully cleaned, heated to the appropriated temperature (20 or 40 °C) with an external water bath, and a fresh air-water interface was created. The surface pressure was monitored during the depositions with an electric balance fitted with a platinum Wilhelmy plate. The substrates were rectangular pieces of ultra-flat silicon wafer ( $\approx 1.1 \times 6$  cm, P100). The substrates were carefully cleaned with distilled water, isopropyl alcohol and ultrasonica-

tion. They were mounted to the dipper arm of the Langmuir-Blodgett trough with an inclination with respect to the liquid interface of about 25 °. After moving the substrate to the starting position, the microgels were spread at the air-water interface. For this purpose, microgels were suspended either in 50/50 vol% mixtures of water-propan-2-ol or in pure chloroform. This was done to maximize the adsorption of the microgels to air-water interfaces and minimize partial loss of microgels into the sub-phase. This loss is unavoidable if the surface-active component is soluble in either phase. After equilibration for at least 30 minutes, the substrates were lifted through the interface while the barriers of the Langmuir-Blodgett trough compressed the interface. The speed of the barriers ( $v_{\text{barrier}} = 6.48 \text{ cm}^2 \text{ min}^{-1}$ ) was matched to the speed of the dipper arm ( $v_{\text{dipper}} = 0.15 \text{ mm min}^{-1}$ ). This, together with the tilt of the substrate, allowed the microgels to be deposited on the substrate with increasing concentration.<sup>33</sup>

## Atomic force microscopy

Deposited, dried microgels were imaged using a Dimension Icon atomic force microscope with closed loop (Veeco Instruments Inc., USA, Software: Nanoscope 9.4, Bruker Co., USA) in tapping mode. The probes were OTESPA tips with a resonance frequency of 300 kHz, a nominal spring constant of 26 N m<sup>-1</sup> of the cantilever and a nominal tip radius of < 7 nm (Opus by Micromasch, Germany).

## Image analysis

The open-source analysis software Gwyddion 2.54 was used to process the AFM images. All images were leveled to remove the tilt and zero height was fixed as the minimum z-value of the image.

Height profiles of single dried microgels were extracted through their apices and at different angles with respect to the fast scan direction. Multiple height profiles of one image were summarized and aligned to the apices (zero coordinate of the x-axis) to obtain averaged microgel

profiles and not to bias the results. The profiles are presented with standard deviations as the error. The apices and heights of microgels were computed using the Matlab function `findpeaks`.

The AFM phase images were used to determine the interfacial (dry) diameter,  $2R_{2D}$ , of the all microgels and the interfacial (dry) diameter of the core,  $2R_{2D,c}$ , of the standard microgels. For this, the interfacial areas,  $A_{2D}$  and  $A_{2D,core}$ , of at least 200 well separated, isolated, and uncompressed microgels were measured.  $2R_{2D}$  and  $2R_{2D,c}$  were calculated by  $2R_{2D} = \sqrt{(4 \cdot A_{2D})/\pi}$

## Specular neutron reflectometry

Specular neutron reflectometry measurements were conducted on FIGARO, a time-of-flight reflectometer at the Institute Laue-Langevin, Grenoble, France. Two angles of incidence ( $\theta_{in} = 0.615$  and  $3.766^\circ$ ) and a wavelength resolution of  $7\% \Delta\lambda/\lambda$  were used yielding a momentum transfer of  $0.089 < Q < 3.5 \text{ nm}^{-1}$ , normal to the interface. The wavelength of the neutron beam,  $\lambda$ , was 0.2 to 3 nm.

An area of  $\approx 10 \times 40 \text{ mm}^2$  was illuminated with the neutron beam. The reflected neutrons were detected by a two-dimensional  $^3\text{He}$  detector. The raw time-of-flight experimental data at these two angles of incidence were calibrated with respect to the incident wavelength distribution and the efficiency of the detector. Using COSMOS,<sup>80</sup> in the framework of LAMPS,<sup>81</sup> this yielded the resulting reflectivity profiles  $R(Q)$ , where  $R$  is defined as the ratio of the intensity of the neutrons scattered at the air-water interface over the incident intensity of the neutron beam.

SNR experiments were performed using  $\text{D}_2\text{O}$  and 8.92% v/v  $\text{D}_2\text{O}:\text{H}_2\text{O}$  mixtures as sub-phase. The latter is generally known as air contrast matched water (ACMW) since its scattering length density is equal to the one of air. A polytetrafluoroethylene (PTFE) Langmuir trough with an area of  $100 \text{ cm}^2$  and a volume of  $\approx 60 \text{ mL}$  equipped with two parallel moving PTFE barriers was used. The trough was placed inside an gas-tight box with heated

sapphire or quartz glass windows to prevent condensation. The box is placed on an active anti-vibration stage which can be moved vertically and horizontally. Prior to a measurement series (measurements at different temperatures), the trough was carefully cleaned and a fresh air-water ( $\text{D}_2\text{O}$  or ACMW) interface was created. For temperature control, the trough was connected to an external water bath. The trough was cooled down to the lowest temperature and left to equilibrate for 30 mins. The microgels were added to the interface from solution with a concentration of  $1 \text{ mg mL}^{-1}$  in deuterated chloroform or 50/50 vol% mixtures of water-propan-2-ol. Subsequently, the interface was compressed to  $\approx 13 \text{ mN m}^{-1}$  and the first measurement was conducted. At this surface pressure the average nearest neighbour distance between the microgels is  $\approx 500 \text{ nm}$  as determined from AFM, see Supplementary Fig. 5. Afterwards the trough was tempered to the next temperature, left to equilibrate for 30 mins, and subsequently a measurement conducted. This was repeated until  $40^\circ\text{C}$  was reached. A feedback loop controlled and adjusted the surface pressure during the experiments. Surface pressures were measured with electric balances equipped with paper Wilhelmy plates.

In the literature it is shown that the polymer fraction within a ULC microgels in bulk is much lower than for cross-linked microgels.<sup>39,54,72</sup> As a consequence, their contrast is very low both in the bulk and at the interface, and long measurement times would be required to collect statistically reliable data. For this reason, only deuterated ULC microgel were measured at the interface. The substitution of 3 atoms of hydrogen with 3 atoms of deuterium improves the contrast of the ULC microgels when both ACMW and pure  $\text{D}_2\text{O}$  are used for the water-phase.

## Analysis and model for neutron reflectometry data

As mentioned above, SNR allowed us to determine the density profile of the microgel monolayer in-situ along the z-direction, normal to the interface. The measured  $R(Q)$  profile can be

linked to an in-plane averaged scattering length density (SLD) profile of the monolayer along the  $z$ -direction,  $b(z)$ , thus giving information of a statistically significant number of microgels.

Here, SNR data modeling was performed by minimizing the difference between the experimental and the calculated reflectivity profile using the Parratt’s recursive formalism.<sup>82</sup> The calculated profiles were obtained under the assumption that the  $z$ -profile of the SLD can be decomposed in  $N$ -layers, with an error function connecting adjacent layers. Every layer was characterized by a constant scattering length density  $b_i$ , which depends on the volume fraction of polymer and solvent in this layer. Data analysis was performed using constraints between layer parameters (thickness, roughness, and degree of hydration or SLD) and simultaneous co-refinement of data sets at two contrasts ( $D_2O$  and ACMW) to reduce ambiguity in modeling with Motofit<sup>83</sup> in IGOR Pro (Wavemetrics). Thus, all parameters in Table 2 and 3, except  $b_i$ , were co-refined for the two contrasts. The model was fitted to the data using global minimization of a least squares function  $\chi^2$ . In each  $i$ -layer, the SLD and the polymer fraction  $x$  follows  $b_i = xb_{\text{pNIPAM}} + (1 - x)b_{\text{solvent}}$ , where  $b_{\text{pNIPAM}}$  and  $b_{\text{solvent}}$  are the theoretically calculated values. The polymer fraction distribution  $x(z)$  normal to the plane of the interface for each  $i$ -layer was calculated as the sum of two error functions as follows

$$x(z) = \frac{1}{2}x_i \left[ \operatorname{erf} \left( \frac{z - d_i/2}{\sqrt{2}\sigma_i} \right) - \operatorname{erf} \left( \frac{z + d_i/2}{\sqrt{2}\sigma_{i+1}} \right) \right], d_i < z < d_{i+1} \quad (1)$$

where,  $d_i$  represents the length of the layer with scattering length density  $b_i$ . The roughness between two layers is given by  $\sigma_i$ .  $\sigma_i$  denotes the roughness of a layer  $i$  with the layer above  $i - 1$ . A similar model has been successfully used to fit NR-curves of pNIPAM nanogels.<sup>44,46</sup>

For the regular microgels,  $N$  was chosen equal four to satisfactory fit the experimental curves. In contrast, good fits of the R(Q)s of monolayer of ultra-low cross-linked microgels were obtained using three layer. Additionally, to demonstrate that a Fresnel reflectivity calculation of a slab model that includes Gaussian error function connecting the layers is valid even in our case, where the ob-

tained roughness values are of the order of the layer thicknesses, an alternative model based on a continuous variation of the SLD profile was used. The SLD profiles were divided into many thin layers (1.5 Å), which sustain the same physical polymer fraction distribution. The results are compared in the Supplementary Information, Supplementary Figs. 10a-d. In particular, two sets of data (5 mol% D7 and ULC D3) were fitted with this alternative method (see Supplementary Information) yielding similar results and, therefore, validating the findings from the different slab-models used.

## Computer simulations

**Standard and ULC microgels modeling** Individual microgels were obtained by self-assembling a binary mixture of patchy particles with valence two and four<sup>71</sup> mimicking the NIPAM monomers and the BIS cross-linkers, respectively. The assembly was carried out through the OXDNA simulation package.<sup>84</sup> Standard microgels were created from a total number of monomers  $N \approx 42000$  within a sphere with the radius  $Z = 100\sigma_m$ , where  $\sigma_m$  is the unit of length in simulations. The cross-linkers, whose concentration was set to be the 5% of the total number of monomers, experienced an additional designing force during the assembly so that they were more densely distributed in the center of the particle. The effect of this additional force has been extensively studied in previous works.<sup>85</sup> For ultra-low-cross-linked (ULC) microgels, we used  $N \approx 21000$  and a sphere with  $Z = 55.5\sigma_m$ , as determined from the comparison of the form factors in bulk. In this case, the number of cross-linkers was set to 0.3% of the total number of monomers. In both standard and ULC microgels, the assembly was carried out until  $> 99.9\%$  of the possible bonds in the network were formed.

At this stage, reversible patchy interactions were made permanent by allowing the microgel beads to interact via the Kremer-Grest model,<sup>86</sup> according to which all beads interact via the Weeks-Chandler-Anderson (WCA) potential:

$$V_{\text{WCA}}(r) = \begin{cases} 4\epsilon \left[ \left( \frac{\sigma_m}{r} \right)^{12} - \left( \frac{\sigma_m}{r} \right)^6 \right] + \epsilon & \text{if } r \leq 2^{\frac{1}{6}}\sigma_m \\ 0 & \text{otherwise.} \end{cases} \quad (2)$$

where  $\epsilon$  sets the energy scale and  $r$  is the distance between two particles. Connected beads interacted also via the Finitely Extensible Nonlinear Elastic

(FENE) potential,

$$V_{\text{FENE}}(r) = -\epsilon k_F R_0^2 \ln \left[ 1 - \left( \frac{r}{R_0 \sigma_m} \right)^2 \right] \text{ if } r < R_0 \sigma_m, \quad (3)$$

with  $k_F = 15$  which determines the stiffness of the bond and  $R_0 = 1.5$  is the maximum bond distance.

To account for the responsivity of the microgel at different temperatures, monomers also interact via an additional potential

$$V_\alpha(r) = \begin{cases} -\epsilon\alpha & \text{if } r \leq 2^{1/6}\sigma_m \\ \frac{1}{2}\alpha\epsilon \left\{ \cos \left[ \gamma \left( \frac{r}{\sigma_m} \right)^2 + \beta \right] - 1 \right\} & \text{if } 2^{1/6}\sigma_m < r \leq R_0\sigma_m \\ 0 & \text{if } r > R_0\sigma_m \end{cases} \quad (4)$$

with  $\gamma = \pi \left( \frac{9}{4} - 2^{1/3} \right)^{-1}$  and  $\beta = 2\pi - \frac{9}{4}\gamma$ .<sup>87</sup>  $V_\alpha$  introduces an effective attraction among polymer beads, modulated by the parameter  $\alpha$ , whose increase allows to mimic the collapse of the microgel observed at high temperatures.

**Behavior at the interface** To investigate the behavior of a microgel adsorbed at an interface, we reproduced the effects of the surface tension by placing a microgel between two fluids. Such fluids were modeled with soft beads within the dissipative particle dynamics (DPD) framework.<sup>88,89</sup> The total interaction force among beads is  $\vec{F}_{ij} = \vec{F}_{ij}^C + \vec{F}_{ij}^D + \vec{F}_{ij}^R$ , where:

$$\vec{F}_{ij}^C = a_{ij} w(r_{ij}) \hat{r}_{ij} \quad (5)$$

$$\vec{F}_{ij}^D = -\gamma w^2(r_{ij}) (\vec{v}_{ij} \cdot \vec{r}_{ij}) \hat{r}_{ij} \quad (6)$$

$$\vec{F}_{ij}^R = 2\gamma \frac{k_B T}{m} w(r_{ij}) \frac{\theta}{\sqrt{\Delta t}} \hat{r}_{ij} \quad (7)$$

where  $\vec{F}_{ij}^C$  is a conservative repulsive force, with  $w(r_{ij}) = 1 - r_{ij}/r_c$  for  $r_{ij} < r_c$  and 0 elsewhere,  $\vec{F}_{ij}^D$  and  $\vec{F}_{ij}^R$  are a dissipative and a random contribution of the DPD, respectively;  $a_{ij}$  quantifies the repulsion between two particles,  $\gamma = 2.0$  is a friction coefficient,  $\theta$  is a Gaussian random variable with zero average and unit variance, and  $\Delta t = 0.002$  is the integration time-step. Following previous works,<sup>10,37</sup> we chose  $a_{11} = a_{22} = 8.8$ ,  $a_{12} = 31.1$ , for the interactions between fluid 1 and fluid 2. Instead, for the monomer-solvent interactions we chose  $a_{m1} = 4.5$  and  $a_{m2} = 5.0$ . In this way, we made fluid 1 the preferred phase for the microgel particle. The cut-off radius was always set to be  $r_c = 1.9\sigma_m$  and the reduced solvent density  $\rho_{\text{DPD}} = 4.5$ . In this way, the total number of par-

ticles was about  $2.6 \times 10^6$  for simulating standard microgels and  $\approx 5.3 \times 10^6$  for ULC microgels. The reduced temperature of the system  $T^*$  was fixed to 1 via the DPD thermostat. We note that by adjusting  $V_\alpha$  to reproduce the effect of temperature on the microgel, we did not change the feature of the interface, which remains defined by the DPD parameters listed above. Simulations were performed with the LAMMPS simulation package.<sup>90</sup>

## Data availability

Raw data were generated at the Institute Laue-Langevin (ILL, Grenoble, France) using the Fluid Interfaces Grazing Angles Reflectometer (FIGARO). The NR raw data used in this study are available in the ILL Data Portal database under accession code 10.5291/ILL-DATA.9-11-1871<sup>91</sup> and 10.5291/ILL-DATA.EASY-462.<sup>92</sup> The raw data, associated data, and derived data supporting the results of this study have been deposited in the RADAR4Chem database under DOI:10.22000/603<sup>93</sup> or are available from the corresponding author at the link <http://hdl.handle.net/21.11102/b0e200f4-d196-44bd-874a-2f5f79d22527>.



# References

- (1) Van Der Scheer, P., Van De Laar, T., Van Der Gucht, J., Vlassopoulos, D. & Sprakel, J. Fragility and strength in nanoparticle glasses. *ACS Nano* **11**, 6755-6763 (2017).
- (2) Keidel, R., Ghavami, A., Lugo, D., Lotze, G., Virtanen, O., Beumers, P., Pedersen, J., Bardow, A., Winkler, R. & Richtering, W. Time-resolved structural evolution during the collapse of responsive hydrogels: The microgel-to-particle transition. *Science Advances* **4**, eaao7086 (2018).
- (3) Brijitta, J. & Schurtenberger, P. Responsive hydrogel colloids: Structure, interactions, phase behavior, and equilibrium and nonequilibrium transitions of microgel dispersions. *Current Opinion In Colloid & Interface Science* **40**, 87-103 (2019).
- (4) Karg, M., Pich, A., Hellweg, T., Hoare, T., Lyon, L., Crassous, J., Suzuki, D., Gumerov, R., Schneider, S., Potemkin, I. & Richtering, W. Nanogels and microgels: From model colloids to applications, recent developments, and future trends. *Langmuir* **35**, 6231-6255 (2019).
- (5) Scheffold, F. Pathways and challenges towards a complete characterization of microgels. *Nature Communications* **11**, 1-13 (2020).
- (6) Geisel, K., Isa, L. & Richtering, W. Unraveling the 3D localization and deformation of responsive microgels at oil/water interfaces: A step forward in understanding soft emulsion stabilizers. *Langmuir* **28**, 15770-15776 (2012).
- (7) Rey, M., Fernandez-Rodriguez, M., Karg, M., Isa, L. & Vogel, N. Poly-N-isopropylacrylamide nanogels and microgels at fluid interfaces. *Accounts Of Chemical Research* **53**, 414-424 (2020).
- (8) Destribats, M., Lapeyre, V., Wolfs, M., Sellier, E., Leal-Calderon, F., Ravaine, V. & Schmitt, V. Soft microgels as Pickering emulsion stabilisers: Role of particle deformability. *Soft Matter* **7**, 7689-7698 (2011).
- (9) Fernandez-Rodriguez, M., Martin-Molina, A. & Maldonado-Valderrama, J. Microgels at interfaces, from mickering emulsions to flat interfaces and back. *Advances In Colloid And Interface Science* , 102350 (2020).
- (10) Camerin, F., Fernández-Rodriguez, M., Rovigatti, L., Antonopoulou, M., Gnan, N., Ninarello, A., Isa, L. & Zaccarelli, E. Microgels adsorbed at liquid-liquid interfaces: A joint numerical and experimental study. *ACS Nano* **13**, 4548-4559 (2019).
- (11) Minato, H., Murai, M., Watanabe, T., Matsui, S., Takizawa, M., Kureha, T. & Suzuki, D. The deformation of hydrogel microspheres at the air/water interface. *Chemical Communications* **54**, 932-935 (2018).
- (12) Cox, J., Yu, K., Constantine, B., Eisenberg, A. & Lennox, R. Polystyrene- poly (ethylene oxide) diblock copolymers form well-defined surface aggregates at the air/water interface. *Langmuir* **15**, 7714-7718 (1999).
- (13) Cox, J., Bruce Lennox, R. & Others Compression of polystyrene-poly (ethylene oxide) surface aggregates at the air/water interface. *Physical Chemistry Chemical Physics* **1**, 4417-4421 (1999).
- (14) Zhang, J. & Pelton, R. Poly (N-isopropylacrylamide) microgels at the air- water interface. *Langmuir* **15**, 8032-8036 (1999).
- (15) Fameau, A., Carl, A., Saint-Jalmes, A. & Von Klitzing, R. Responsive aqueous foams. *ChemPhysChem* **16**, 66-75 (2015).

- (16) Wu, D., Mihali, V. & Honciuc, A. pH-responsive pickering foams generated by surfactant-free soft hydrogel particles. *Langmuir* **35**, 212-221 (2018).
- (17) Horiguchi, Y., Kawakita, H., Ohto, K. & Morisada, S. Temperature-responsive Pickering foams stabilized by poly (N-isopropylacrylamide) nanogels. *Advanced Powder Technology* **29**, 266-272 (2018).
- (18) Ngai, T., Behrens, S. & Auweter, H. Novel emulsions stabilized by pH and temperature sensitive microgels. *Chemical Communications*, 331-333 (2005).
- (19) Brugger, B., Rosen, B. & Richtering, W. Microgels as stimuli-responsive stabilizers for emulsions. *Langmuir* **24**, 12202-12208 (2008).
- (20) Fujii, S., Read, E., Binks, B. & Armes, S. Stimulus-responsive emulsifiers based on nanocomposite microgel particles. *Advanced Materials* **17**, 1014-1018 (2005).
- (21) Bochenek, S., McNamee, C., Kappl, M., Butt, H. & Richtering, W. Interactions between a responsive microgel monolayer and a rigid colloid: from soft to hard interfaces. *Physical Chemistry Chemical Physics* **23**, 16754-16766 (2021).
- (22) Nerapusri, V., Keddie, J., Vincent, B. & Bushnak, I. Swelling and deswelling of adsorbed microgel monolayers triggered by changes in temperature, pH, and electrolyte concentration. *Langmuir* **22**, 5036-5041 (2006).
- (23) Schmidt, S., Zeiser, M., Hellweg, T., Duschl, C., Fery, A. & Möhwald, H. Adhesion and mechanical properties of PNIPAM microgel films and their potential use as switchable cell culture substrates. *Advanced Functional Materials* **20**, 3235-3243 (2010).
- (24) Cors, M., Wiehemeier, L., Hertle, Y., Feoktystov, A., Cousin, F., Hellweg, T. & Oberdisse, J. Determination of internal density profiles of smart acrylamide-based microgels by small-angle neutron scattering: A multishell reverse monte carlo approach. *Langmuir* **34**, 15403-15415 (2018).
- (25) Schulte, M., Bochenek, S., Brugnoli, M., Scotti, A., Mourran, A. & Richtering, W. Stiffness tomography of ultra-soft nanogels by atomic force microscopy. *Angewandte Chemie International Edition* **60**, 2280-2287 (2021).
- (26) Richtering, W. Responsive emulsions stabilized by stimuli-sensitive microgels: emulsions with special non-Pickering properties. *Langmuir* **28**, 17218-17229 (2012).
- (27) Lefroy, K., Murray, B. & Ries, M. Advances in the use of microgels as emulsion stabilisers and as a strategy for cellulose functionalisation. *Cellulose* **28**, 647-670 (2021).
- (28) Stock, S. & Klitzing, R. Microgels at droplet interfaces of water-in-oil emulsions-challenges and progress. *Current Opinion In Colloid & Interface Science*, 101561 (2022).
- (29) Nguyen, B., Wang, W., Saunders, B., Benyahia, L. & Nicolai, T. pH-responsive water-in-water Pickering emulsions. *Langmuir* **31**, 3605-3611 (2015).
- (30) Monteux, C., Marliere, C., Paris, P., Pantoustier, N., Sanson, N. & Perrin, P. Poly (N-isopropylacrylamide) microgels at the oil- water interface: Interfacial properties as a function of temperature. *Langmuir* **26**, 13839-13846 (2010).
- (31) Faulde, M., Tonn, J. & Jupke, A. Microgels for the intensification of liquid-liquid extraction processes—feasibility and advantages. *Chemical Engineering & Technology* **43**, 137-142 (2020).
- (32) Mehrabian, H., Snoeijer, J. & Harting, J. Desorption energy of soft particles from a fluid interface. *Soft Matter* **16**, 8655-8666 (2020).

- (33) Rey, M., Fernández-Rodríguez, M., Steinacher, M., Scheidegger, L., Geisel, K., Richtering, W., Squires, T. & Isa, L. Isostructural solid–solid phase transition in monolayers of soft core–shell particles at fluid interfaces: structure and mechanics. *Soft Matter* **12**, 3545–3557 (2016).
- (34) Bochenek, S., Scotti, A., Ogieglo, W., Fernández-Rodríguez, M., Schulte, M., Gumerov, R., Bushuev, N., Potemkin, I., Wessling, M., Isa, L. & Richtering, W. Effect of the 3D swelling of microgels on their 2D phase behavior at the liquid–liquid interface. *Langmuir* **35**, 16780–16792 (2019).
- (35) Harrer, J., Rey, M., Ciarella, S., Löwen, H., Janssen, L. & Vogel, N. Stimuli-responsive behavior of PNIPAm microgels under interfacial confinement. *Langmuir* **35**, 10512–10521 (2019).
- (36) Bochenek, S., Scotti, A. & Richtering, W. Temperature-sensitive soft microgels at interfaces: air–water versus oil–water. *Soft Matter* **17**, 976–988 (2021).
- (37) Camerin, F., Gnan, N., Ruiz-Franco, J., Ninarello, A., Rovigatti, L. & Zaccarelli, E. Microgels at interfaces behave as 2D elastic particles featuring reentrant dynamics. *Physical Review X* **10**, 031012 (2020).
- (38) Schulte, M., Scotti, A., Brugnioni, M., Bochenek, S., Mourran, A. & Richtering, W. Tuning the structure and properties of ultra-low cross-linked temperature-sensitive microgels at interfaces via the adsorption pathway. *Langmuir* **35**, 14769–14781 (2019).
- (39) Scotti, A., Bochenek, S., Brugnioni, M., Fernandez-Rodríguez, M., Schulte, M., Houston, J., Gelissen, A., Potemkin, I., Isa, L. & Richtering, W. Exploring the colloid-to-polymer transition for ultra-low crosslinked microgels from three to two dimensions. *Nature Communications* **10**, 1418 (2019).
- (40) Vialetto, J., Camerin, F., Grillo, F., Ramakrishna, S., Rovigatti, L., Zaccarelli, E. & Isa, L. Effect of internal architecture on the assembly of soft particles at fluid interfaces. *ACS Nano* **15**, 13105–13117 (2021).
- (41) Ciarella, S., Rey, M., Harrer, J., Holstein, N., Ickler, M., Lowen, H., Vogel, N. & Janssen, L. Soft particles at liquid interfaces: From molecular particle architecture to collective phase behavior. *Langmuir* **37**, 5364–5375 (2021).
- (42) Menath, J., Eatson, J., Brilmayer, R., Andrieu-Brunsen, A., Buzza, D. & Vogel, N. Defined core–shell particles as the key to complex interfacial self-assembly. *Proceedings Of The National Academy Of Sciences* **118** (2021).
- (43) Grillo, F., Fernandez-Rodríguez, M., Antonopoulou, M., Gerber, D. & Isa, L. Self-templating assembly of soft microparticles into complex tessellations. *Nature* **582**, 219–224 (2020).
- (44) Zielińska, K., Sun, H., Campbell, R., Zarbakhsh, A. & Resmini, M. Smart nanogels at the air/water interface: structural studies by neutron reflectivity. *Nanoscale* **8**, 4951–4960 (2016).
- (45) Richardson, R., Pelton, R., Cosgrove, T. & Zhang, J. A Neutron reflectivity study of poly (N-isopropylacrylamide) at the air–water interface with and without sodium dodecyl sulfate. *Macromolecules* **33**, 6269–6274 (2000).
- (46) Zielińska, K., Campbell, R., Zarbakhsh, A. & Resmini, M. Adsorption versus aggregation of NIPAM nanogels: new insight into their behaviour at the air/water interface as a function of concentration. *Physical Chemistry Chemical Physics* **19**, 17173–17179 (2017).
- (47) Mourran, A., Wu, Y., Gumerov, R., Rudov, A., Potemkin, I., Pich, A. & Möller, M. When colloidal particles become polymer coils. *Langmuir* **32**, 723–730 (2016).

- (48) Schmidt, S., Liu, T., Rütten, S., Phan, K., Möller, M. & Richtering, W. Influence of microgel architecture and oil polarity on stabilization of emulsions by stimuli-sensitive core-shell poly (N-isopropylacrylamide-co-methacrylic acid) microgels: Mickering versus Pickering behavior? *Langmuir* **27**, 9801-9806 (2011).
- (49) M. Stieger, W. Richtering, S. Pedersen, J. & P. Lindner Small-angle neutron scattering study of structural changes in temperature sensitive microgel colloids. *The Journal Of Chemical Physics* **120**, 6197-6206 (2004).
- (50) Pelton, R. & Chibante, P. Preparation of aqueous lattices with N-isopropylacrylamide. *Colloids And Surfaces* **20**, 247-256 (1986).
- (51) Gao, J. & Frisken, B. Cross-linker-free N-isopropylacrylamide gel nanospheres. *Langmuir* **19**, 5212-5216 (2003).
- (52) Brugnoli, M., Nickel, A., Kröger, L., Scotti, A., Pich, A., Leonhard, K. & Richtering, W. Synthesis and structure of deuterated ultra-low cross-linked poly (N-isopropylacrylamide) microgels. *Polymer Chemistry* **10**, 2397-2405 (2019).
- (53) Houston, J. E., Fruhner, L., de la Cotte, A., Rojo González, J., Petrunin, A., Gasser, U., Schweins, R., Allgaier, J., Richtering, W., Fernandez-Nieves, A. & Scotti A. Resolving the different bulk moduli within individual soft nanogels using small-angle neutron scattering. *Science Advances* **8**, eabn6129 (2022).
- (54) Islam, M., Nguyen, R. & Lyon, L. Emergence of non-hexagonal crystal packing of deswollen and deformed ultra-soft microgels under osmotic pressure control. *Macromolecular Rapid Communications* **42**, 2100372 (2021).
- (55) Scotti, A., Houston, J., Brugnoli, M., Schmidt, M., Schulte, M., Bochenek, S., Schweins, R., Feoktystov, A., Radulescu, A. & Richtering, W. Phase behavior of ultrasoft spheres show stable bcc lattices. *Physical Review E* **102**, 052602 (2020).
- (56) Scotti, A. Characterization of the volume fraction of soft deformable microgels by means of small-angle neutron scattering with contrast variation. *Soft Matter* **17**, 5548-5559 (2021)
- (57) Scotti, A., Denton, A., Brugnoli, M., Houston, J., Schweins, R., Potemkin, I. & Richtering, W. Deswelling of microgels in crowded suspensions depends on cross-Link density and architecture. *Macromolecules* **52**, 3995-4007 (2019).
- (58) Flory, P. & Rehner, J. Statistical mechanics of cross-linked polymer networks I. rubberlike elasticity. *The Journal Of Chemical Physics* **11**, 512-520 (1943).
- (59) Flory, P. & Rehner, J. Statistical mechanics of cross-linked polymer networks II. swelling. *The Journal Of Chemical Physics* **11**, 521-526 (1943).
- (60) Lopez, C. & Richtering, W. Does Flory-Rehner theory quantitatively describe the swelling of thermoresponsive microgels? *Soft Matter* **13**, 8271-8280 (2017).
- (61) Shirota, H., Kuwabara, N., Ohkawa, K. & Horie, K. Deuterium isotope effect on volume phase transition of polymer gel: Temperature dependence. *The Journal Of Physical Chemistry B* **103**, 10400-10408 (1999).
- (62) Shirota, H. & Horie, K. Deuterium isotope effect on swelling process in aqueous polymer gels. *Chemical Physics* **242**, 115-121 (1999).
- (63) Cors, M., Wiehemeier, L., Oberdisse, J. & Hellweg, T. Deuteration-induced volume phase transition temperature shift of PNIPMAM microgels. *Polymers* **11**, 620 (2019).

- (64) Buratti, E., Tavagnacco, L., Zanatta, M., Chiessi, E., Buoso, S., Franco, S., Ruzicka, B., Angelini, R., Orecchini, A., Bertoldo, M. & Others. The role of polymer structure on water confinement in poly (N-isopropylacrylamide) dispersions. *Journal Of Molecular Liquids* **355**, 118924 (2022).
- (65) Maestro, A. & Gutfreund, P. In situ determination of the structure and composition of Langmuir monolayers at the air/water interface by neutron and X-ray reflectivity and ellipsometry. *Advances In Colloid And Interface Science* **293**, 102434 (2021).
- (66) Geisel, K., Henzler, K., Guttman, P. & Richtering, W. New insight into microgel-stabilized emulsions using transmission x-ray microscopy: nonuniform deformation and arrangement of microgels at liquid interfaces. *Langmuir* **31**, 83-89 (2014).
- (67) Destribats, M., Lapeyre, V., Sellier, E., Leal-Calderon, F., Schmitt, V. & Ravaine, V. Water-in-oil emulsions stabilized by water-dispersible poly (N-isopropylacrylamide) microgels: Understanding anti-Finkle behavior. *Langmuir* **27**, 14096-14107 (2011).
- (68) Geisel, K., Rudov, A., Potemkin, I. & Richtering, W. Hollow and core-shell microgels at oil-water interfaces: Spreading of soft particles reduces the compressibility of the monolayer. *Langmuir* **31**, 13145-13154 (2015).
- (69) Kleinschmidt, D., Nothdurft, K., Anakhov, M., Meyer, A., Mork, M., Gumerov, R., Potemkin, I., Richtering, W. & Pich, A. Microgel organocatalysts: Modulation of reaction rates at liquid-liquid interfaces. *Materials Advances* **1**, 2983-2993 (2020).
- (70) Romeo, G., Imperiali, L., Kim, J., Fernández-Nieves, A. & Weitz, D. Origin of de-swelling and dynamics of dense ionic microgel suspensions. *The Journal Of Chemical Physics* **136**, 124905 (2012).
- (71) Gnan, N., Rovigatti, L., Bergman, M. & Zaccarelli, E. In silico synthesis of microgel particles. *Macromolecules* **50**, 8777-8786 (2017).
- (72) Scotti, A., Brugnoli, M., Lopez, C., Bochenek, S., Crassous, J. & Richtering, W. Flow properties reveal the particle-to-polymer transition of ultra-low crosslinked microgels. *Soft Matter* **16**, 668-678 (2020).
- (73) Conley, G., Nöjd, S., Braibanti, M., Schurtenberger, P. & Scheffold, F. Super-resolution microscopy of the volume phase transition of pNIPAM microgels. *Colloids And Surfaces A: Physico-chemical And Engineering Aspects* **499**, 18-23 (2016).
- (74) Andronov, L., Orlov, I., Lutz, Y., Vonesch, J. & Klaholz, B. ClusterViSu, a method for clustering of protein complexes by Voronoi tessellation in super-resolution microscopy. *Scientific Reports* **6**, 1-9 (2016).
- (75) Rubin-Delanchy, P., Burn, G., Griffié, J., Williamson, D., Heard, N., Cope, A. & Owen, D. Bayesian cluster identification in single-molecule localization microscopy data. *Nature Methods* **12**, 1072-1076 (2015).
- (76) Huang, S., Gawlitza, K., Klitzing, R., Gilson, L., Nowak, J., Odenbach, S., Steffen, W. & Auernhammer, G. Microgels at the water/oil interface: In situ observation of structural aging and two-dimensional magnetic bead Microrheology. *Langmuir* **32**, 712-722 (2016).
- (77) Fernandez-Rodriguez, M., Antonopoulou, M. & Isa, L. Near-zero surface pressure assembly of rectangular lattices of microgels at fluid interfaces for colloidal lithography. *Soft Matter* **17**, 335-340 (2021).
- (78) Kralchevsky, P. & Nagayama, K. Capillary interactions between particles bound to interfaces, liquid films and biomembranes. *Advances In Colloid And Interface Science* **85**, 145-192 (2000).

- (79) Vialetto, J., Nussbaum, N., Bergfreund, J., Fischer, P. & Isa, L. Influence of the interfacial tension on the microstructural and mechanical properties of microgels at fluid interfaces. *Journal Of Colloid And Interface Science* **608**, 2584-2592 (2022).
- (80) Gutfreund, P., Saerbeck, T., Gonzalez, M., Pellegrini, E., Laver, M., Dewhurst, C. & Cubitt, R. Towards generalized data reduction on a chopper-based time-of-flight neutron reflectometer. *Journal Of Applied Crystallography* **51**, 606-615 (2018).
- (81) Richard, D., Ferrand, M. & Kearley, G. Lamp, the large array manipulation program. *J. Neutron Res* **4**, 33-39 (1996).
- (82) Parratt, L. Surface studies of solids by total reflection of X-Rays. *Phys. Rev.* **95**, 359-369 (1954).
- (83) Nelson, A. Co-refinement of multiple-contrast neutron/X-ray reflectivity data using MOTOFIT. *Journal Of Applied Crystallography* **39**, 273-276 (2006).
- (84) Rovigatti, L., Šulc, P., Reguly, I. & Romano, F. A comparison between parallelization approaches in molecular dynamics simulations on GPUs. *Journal Of Computational Chemistry* **36**, 1-8 (2015).
- (85) Ninarello, A., Crassous, J., Paloli, D., Camerin, F., Gnan, N., Rovigatti, L., Schurtenberger, P. & Zaccarelli, E. Modeling microgels with a controlled structure across the volume phase transition. *Macromolecules* **52**, 7584-7592 (2019).
- (86) Kremer, K. & Grest, G. Dynamics of entangled linear polymer melts: A molecular-dynamics simulation. *The Journal Of Chemical Physics* **92**, 5057-5086 (1990).
- (87) Soddemann, T., Dünweg, B. & Kremer, K. A generic computer model for amphiphilic systems. *The European Physical Journal E* **6**, 409-419 (2001).
- (88) Groot, R. & Warren, P. Dissipative particle dynamics: Bridging the gap between atomistic and mesoscopic simulation. *J. Chem. Phys.* **107**, 4423-4435 (1997).
- (89) Camerin, F., Gnan, N., Rovigatti, L. & Zaccarelli, E. Modelling realistic microgels in an explicit solvent. *Scientific Reports* **8**, 1-12 (2018).
- (90) Plimpton, S. Fast parallel algorithms for short-range molecular dynamics. *Journal Of Computational Physics* **117**, 1-19 (1995).
- (91) Bochenek, S., Gutfreund P., Lima, L., Maestro, A., Richtering, W., Schmidt, M. M., Scotti, A. Thermo-responsive microgels at air-water interfaces: specular neutronreflectometry study to obtain out-of-plane density profiles. Institut Laue-Langevin Data Portal (ILL Data Portal), doi:10.5291/ILL-DATA.9-11-1871 (2018).
- (92) Bochenek, S., Maestro, A., Scotti, A. Deuterated microgels at the liquid-air interface: Effect of crosslinking and temperature. (Continuation of experiment 9-11-1871). Institut Laue-Langevin Data Portal (ILL Data Portal), doi:10.5291/ILL-DATA.EASY-462 (2019).
- (93) Bochenek, S., Camerin, F., Zaccarelli, E., Maestro, A., Schmidt, M. M., Richtering, W., Scotti, A. Dataset: In-situ study of the impact of temperature and architecture on the interfacial structure of thermo-responsive microgels. RADAR4Chem, doi:10.22000/603 (2022).

## Acknowledgements

The authors thank Yuri Gerelli for valuable discussions and Monia Burgnoni for synthesis of the deuterated microgels. SB, MMS, WR and AS acknowledge funding from the Deutsche Forschungsgemeinschaft within SFB 985 "Functional Microgels and Microgel Systems", projects A3 and B8. FC and EZ acknowledge financial support from the European Research Council (Consolidator Grant 681597, MIMIC). This work is based upon NR experiments performed at the Institute Laue-Langevin (ILL, Grenoble, France) using the Fluid Interfaces Grazing Angles Reflectometer (FIGARO). This work is partially based on SANS experiments performed at the D11 instrument at the Institut Laue-Langevin (ILL), Grenoble, France and at the KWS-2 instrument operated by JCNS at the Heinz Maier-Leibnitz Zentrum (MLZ), Garching, Germany.

## Author contributions statement

W.R., A.S., E.Z., F.C., and S.B. designed this study. A.S., M.S., A.M., and S.B. performed the NR measurements. A.S., A.M. and S.B. designed the model for the NR data. A.M. and S.B. analyzed the NR data. S.B. synthesized and characterized the hydrogenated microgels. S.B. performed Langmuir-Blodgett and AFM measurements. S.B. analyzed the AFM data. F.C. performed the computer simulations. All authors participated in discussing the results, writing, finalizing, and revising the manuscript.

## Competing interests statement

The authors declare no competing interests.